



Synthesis of S-Doped porous g-C₃N₄ by using ionic liquids and subsequently coupled with Au-TiO₂ for exceptional cocatalyst-free visible-light catalytic activities

Fazal Raziq^{a,1}, Muhammad Humayun^{b,1}, Asad Ali^d, Tingting Wang^c, Abbas Khan^d, Qiuyun Fu^b, Wei Luo^{b,*}, Heping Zeng^{c,*}, Zhiping Zheng^b, Bilawal Khan^a, Huahai Shen^e, Xiaotao Zu^f, Sean Li^g, Liang Qiao^{a,g,*}

^a School of Physics, University of Electronic Science and Technology of China, Chengdu, 610054, PR China

^b Engineering Research Center for Functional Ceramics of the Ministry of Education, School of Optical and Electronic Information, Huazhong University of Science and Technology, Wuhan, 430074, PR China

^c Key Laboratory of Functional Molecular Engineering of Guangdong Province, School of Chemistry and Chemical Engineering, South China University of Technology, Guangzhou, 510640, PR China

^d Department of Chemistry, Abdul Wali Khan University Mardan, 23200, KP, Pakistan

^e Institute of Nuclear Physics and Chemistry, Chinese Academy of Engineering Physics, Mianyang, 621900, PR China

^f Institute of Fundamental and Frontier of Sciences, University of Electronic Science and Technology of China, Chengdu 610054, PR China

^g School of Materials, University of New South Wales, Sydney, 2052, NSW Australia

ARTICLE INFO

Keywords:

Solar fuel
Charge separation
CO₂ conversion
Water splitting
2,4-DCP degradation

ABSTRACT

The development of new technologies for carbon dioxide reduction, water splitting, and pollutant degradation has been a demanding challenge in the globe due to critical energy and environmental issues. Herein, we have successfully synthesized sulfur doped porous g-C₃N₄ (S-PCN) using ionic liquid, and then coupled nanocrystalline anatase TiO₂ and Au-modified TiO₂ to obtain nanocomposites. The amount-optimized 1 Au-6 T/6S-PCN nanocomposite exhibits exceptional visible-light activities for CO₂ conversion to CH₄, H₂ evolution, and 2,4-dichlorophenol degradation, respectively by ~32-time (365 μmol g⁻¹ h⁻¹), ~41-time (330 μmol g⁻¹ h⁻¹) and ~24-time (95% 10 mg h⁻¹ L⁻¹) enhancement compared to the porous g-C₃N₄ (PCN). The calculated quantum efficiencies for CH₄ production and H₂ evolution are ~4.67% and ~3.34% at 420 nm wavelength. Based on these results, it is suggested that the exceptional photoactivities are attributed to the large surface area (100.5 m² g⁻¹), extended visible-light response and enhanced charge separation via dopant induced surface-states and subsequently coupled Au-TiO₂. Furthermore, the ·CO₂ and ·H as active radicals would be dominant to respectively initiate CO₂ and H₂O reduction, and the produced ·OH plays a vital role in 2,4-dichlorophenol degradation. This work demonstrates that the designed PCN-based nanocomposites show promising applications in CO₂ photo-reduction, water splitting, and pollutant degradation.

1. Introduction

The energy crisis and environmental pollution are the burning issues in this planet because human population growth, urbanization, and emergent living standards have swiftly increased the green energy demand over world-wide due to the enormous utilization of fossil fuels such as petroleum, coal, and natural gas [1–3]. The extensive exploitation of these fossil fuels has caused enormous CO₂ emission and undesirable global environmental warming and climate changes. In the

past few decades, the industrial CO₂ emission was estimated to be 280 ppm, but currently the concentration has surpassed 400 ppm which is the main reason of global warming [4–6]. In fact, there is no universal solution to solve these serious issues. However, research communities see hope in the design of new and alternative technologies, which could fulfill the future green energy demands such as sustainable energy production and storage [7,8]. On the other hand, 2,4-dichlorophenol as the highly toxic and persistent environmental pollution has been enlisted by the US environmental protection agency (EPA) as a priority

* Corresponding authors.

E-mail addresses: luowei@mail.hust.edu.cn (W. Luo), hpzeng@scut.edu.cn (H. Zeng), liang.qiao@uestc.edu.cn (L. Qiao).

¹ These authors contributed equally to this work.

control pollutant. It is difficult to biodegrade due to high stability of carbon-chlorine bonds. In the previous decades, electrocatalytic and traditionally biological methods have widely been used to solve energy and environmental issues. However, these methods do not fulfill the requirements of efficient energy production and pollutants degradation. Further, these techniques always exhibit shortfalls such as low mechanical strength, less stability, electrode corrosion, and catalyst poisoning. Hence, it is highly desirable to design and develop alternative techniques to overcome the above mentioned shortcomings [9–11].

Recently, heterogeneous semiconductor-photocatalysis has been considered as a promising and alternative technique to solve both the energy and environmental issues [12]. A great deal of work has been committed to design low cost, efficient, and stable semiconductor photocatalysts for CO₂ reduction, water splitting and pollutant oxidation [13–15]. In this regard, TiO₂ is the mostly investigated semiconductor photocatalyst. However, TiO₂ (band gap, $E_g = 3.2$ eV) can only be photo-excited under UV-light, thus only utilize 3–5% of the solar-spectrum resources [16]. In contrast, the visible light, comprising 46% of the entire solar spectrum, provides tremendous light resources. Hence, it is much meaningful to effectively utilize the solar energy by developing visible-light responsive nanophotocatalysts. Among semiconductor nanophotocatalysts, g-C₃N₄ ($E_g = 2.7$ eV) has attracted significant attention owing to its unique conduction band minimum (CBM = -1.3 eV) and valence band maximum (VBM = 1.4 eV) as well as its intrinsic high chemical stability [17,18]. However, low surface area, poor visible-light response and high recombination rate of photo-generated charges still greatly limit its potential for practical applications. Therefore, it is highly desirable to design and develop new routes to improve the surface area, visible-light response, charge separation, and photocatalytic activities of g-C₃N₄ [19].

To overcome the drawbacks of g-C₃N₄, many strategies such as introducing porous structure, doping elements, and constructing heterojunctions are widely employed [20,21]. Amongst the common non-metal dopants, sulfur is the most attractive one because it has promising applications in the field of material science. Sulfur acts as a donor of electrons and shows different changes at the electronic structure, this is the main reason that sulfur dopant is more competitive as compared to other nonmetals dopants. Hence, Sulfur doping could enhance the visible-light response and charge separation by replacing the C atoms from the ring of porous g-C₃N₄ (PCN) and form a bonded planar layered structure like melon [22–24]. Sulfur doping induces surface states below the CBM of PCN thus providing suitable Fermi-level and efficient charge separation. Therefore, it is assumed that the sulfur related surface states would trap the negatively-charged carriers during photo-excitation. Unfortunately, the origin of sulfur doping induced surface states and working mechanism of subsequent photogenerated charge separation process are not clear up to date. For sulfur doping, here we used ionic liquid because the ionic liquid has high melting and boiling points and do not decompose easily to form volatile products under ambient conditions. Coupling with semiconductor-oxides (such as SnO₂, ZnO, and TiO₂) presents another strategy to improve the photo-induced charge separation of PCN [25–27]. By transferring the visible-light excited electrons of PCN to the conduction band of wide band gap semiconductor oxides, the photocatalytic performance of PCN for CO₂ photoreduction, H₂ evolution, and pollutant degradation could be significantly improved. Moreover, an effective cocatalyst for reduction reactions is also necessary, which would greatly improve the photocatalytic activities of PCN. It is recommended that noble-metals, like Pt, Au, and Ag are always best choice as effective co-catalysts. Wei et al., first prepared g-C₃N₄/TiO₂ composite photocatalysts and subsequently decorated with noble-metals (Au, Ag, or Pt) for efficient water splitting to evolve H₂ [28]. Our recent work also demonstrate that the coupled Au-TiO₂ could work as a dual-functional modifier to improve the catalytic activities as well as charge separation and transfer of PCN [19]. However, such attempts have rarely been made to modify g-C₃N₄ to till date. Therefore, it is a promising idea to simultaneously improve the visible-

light response, charge separation and transfer, as well as photocatalytic performance of PCN by coupling a dual-functional noble-metal-modified wide-band-gap oxide [29–31]. In particular, it is much feasible that the electrons are completely utilized in reduction reactions and the produced holes would directly attack H₂O to evolve O₂. Thus, the oxidation ability of PCN could also be improved.

PCN exhibits graphene like π -conjugated structure. Meanwhile, CO₂ molecules also contain delocalized π -conjugated binding electrons. Thus, a π - π conjugation interaction can be established between PCN and CO₂ [32]. This unique π - π conjugation interaction can drastically improve the adsorption and activation of CO₂ molecules on the PCN-based photocatalysts, thereby improving the photocatalytic CO₂ reduction ability. Further, this π - π conjugation interaction between PCN and CO₂ can also lead to the destabilization and activation of CO₂ molecules, thereby facilitating the CO₂ photo-reduction reactions [33].

Generally, the CO₂ reduction is based on two possible pathways. First, the adsorption of CO₂ forms partially charged species like $\cdot\text{CO}_2$ by interacting with the surface atoms. Although, CO₂ is a linear symmetry molecule and does not exhibit dipole moment. However, the lone-pair electrons of each oxygen atom can be donated to the surface Lewis-acid centers [34,35]. Furthermore, the carbon-atom could accept electrons from the Lewis-base centers like oxide ions, to form carbonate species. Simultaneously, the molecule of CO₂ acts as electronic donor and acceptor bi-functional species and form mix coordination. In addition, the $\cdot\text{CO}_2$ adsorbate does not adopt CO₂-like linear symmetry and exhibit a lower barrier for accepting an electron since the lower unoccupied molecular orbital level decreases as the molecule bends. As a result, one electron reduction would be possible at low energy electrons. Thus, it is possible for the adsorbed CO₂ to be reduced by the low-energy electrons. Secondly, it is closely related to the produced $\cdot\text{H}$, because in present case the production of $\cdot\text{H}$ were confirmed by the overall water splitting measurements [36,37]. Thus the adsorbed CO₂ is gradually transformed into CH₄ and CO.

Based on the above consideration, herein we have used ionic liquid as a source of sulfur to synthesize sulfur doped porous g-C₃N₄ and simultaneously coupled with TiO₂ and Au-TiO₂ to enhance the visible-light photoactivities. It is clearly demonstrated that the exceptional visible-light photocatalytic activities for CO₂ reduction to CH₄, water splitting to evolve H₂, and 2,4-DCP degradation mainly resulted from the extended visible-light response and enhanced charge separation by doping sulfur to create surface states and simultaneously coupling Au-TiO₂. Furthermore, it is demonstrated that the $\cdot\text{CO}_2$ and $\cdot\text{H}$ as active intermediate radicals would be much more favorable to induce the reduction of CO₂ to CH₄. This work provides an efficient strategy to design bifunctional PCN-based nanocomposites with excellent photocatalytic activity for achievable CO₂ photo-reduction, water splitting, and pollutant degradation for environmental remediation.

2. Results and discussion

The crystal structures of the samples were measured with X-ray diffraction (XRD). The XRD patterns of PCN and xS-PCN samples are given in Figure S1 (Supporting Information), while that of 6S-PCN, yT/6S-PCN and 1 Au-6 T/6S-PCN samples are shown in Fig. 1A. The XRD patterns of CN exhibit two characteristic peaks. The more intense and broad peak at $2\theta = 27.4^\circ$ (002 facet) corresponds to the interlayer-stacking interaction of the aromatic systems and mainly found in graphitic materials. While the low-angle one at $2\theta = 13.1^\circ$ (100 facet) corresponds to the in-plane repeated distance of 0.326 nm, that well matches with the dimensions of triazine structures within the layers. From Figure S1 (Supporting Information), it is clear that after doping sulfur, the main peak at $2\theta = 27.4^\circ$ shifts to a lower angle suggesting that sulfur is incorporated into the crystal lattice of PCN [38]. The electronegativity of sulfur is higher than that of carbon but lower than that of nitrogen, thus sulfur can easily substitute carbon atoms. Meanwhile, due to the large size of sulfur atoms, the inter-planar distance

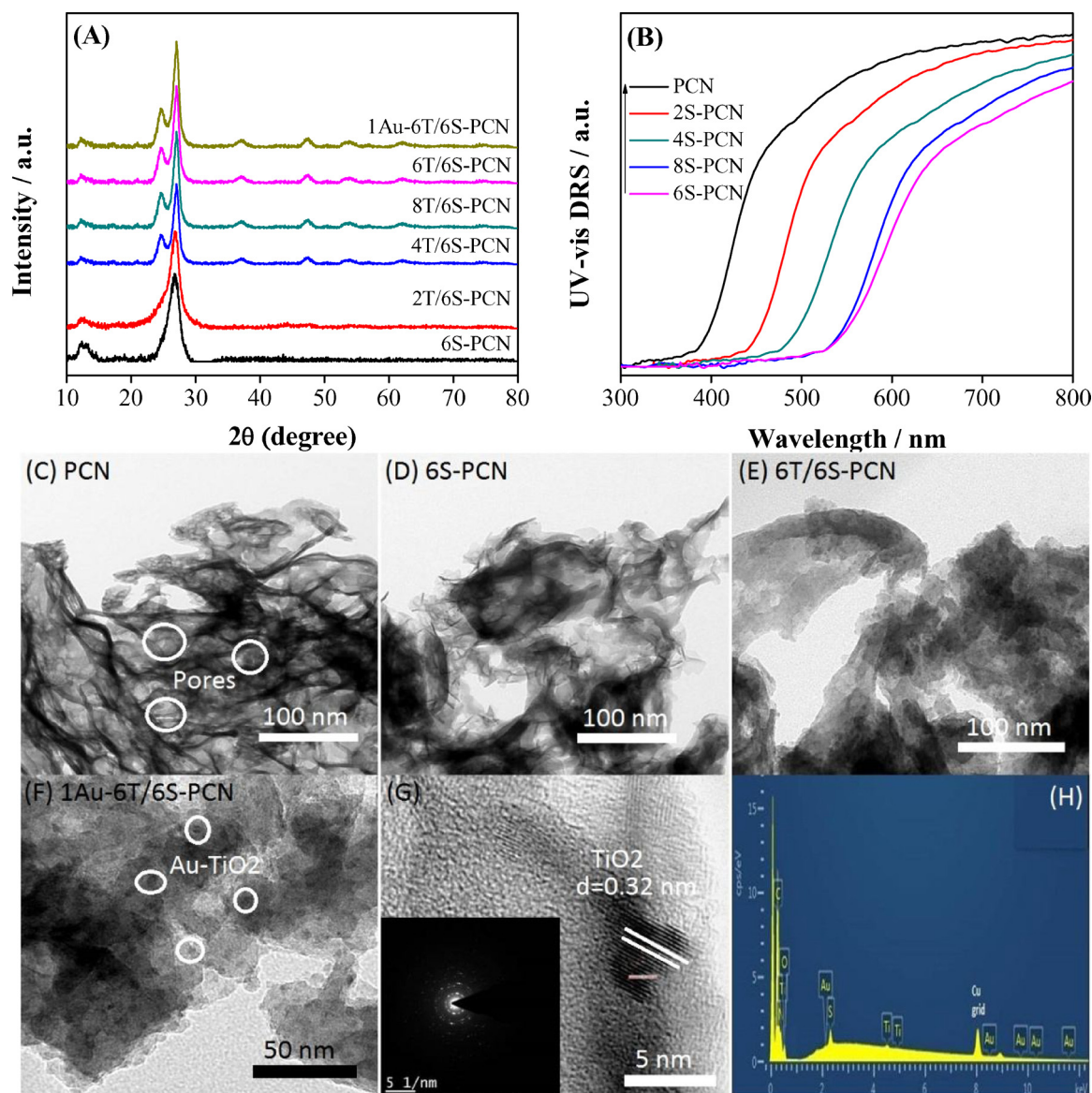


Fig. 1. XRD patterns (A) of 6S-PCN, yT/6S-PCN and 1 Au-6 T/6S-PCN. UV-vis DRS spectra (B) of PCN and xS-PCN. TEM images (C) PCN, (D) 6S-PCN, (E) 6 T/6S-PCN, (F) 1 Au-6 T/6S-PCN and (G) HRTEM image of 1 Au-6 T/6S-PCN nanocomposite with inset SAED patterns of TiO₂. (H) Energy dispersive X-ray spectroscopy spectra of 1 Au-6 T/6S-PCN nanocomposite. Where x and y respectively means different amount of sulfur and TiO₂.

will slightly increase and as a result the main peak of PCN will shift toward lower diffraction angle, as observed. From Fig. 1A, it is obvious that the introduction of TiO₂ does not change the crystal-phase and crystallinity of 6S-PCN sample. However, the TiO₂ characteristic peaks appeared in the XRD patterns of 6S-PCN sample. Further, the intensity of TiO₂ peaks gradually increased with increasing TiO₂ content. Moreover, coupling of 1 Au-TiO₂ has no effect on the crystal-phase of 6S-PCN sample. The XRD peaks of Au did not appear in 1 Au-6 T/6S-PCN nanocomposite due to its small amount.

To investigate the absorption characteristics of the resultant PCN, xS-PCN, yT/6S-PCN and 1 Au-6 T/6S-PCN samples, UV-vis diffuse-reflectance spectra (DRS) were obtained. From Fig. 1B, it is clear that the UV-vis diffuse-reflectance spectra of xS-PCN samples are remarkably shifted toward longer wavelength direction compared to the pure PCN. Hence, it is clear that sulfur doping has greatly extended the visible-light response of PCN and low energy photons are thus able to excite its VB electrons. From Figure S2 (Supporting Information), it is clear that coupling of TiO₂ and 1 Au-TiO₂ would be useful for the visible-light absorption of xS-PCN to a certain level.

The morphology and structural characteristics of PCN, 6S-PCN, 6 T/6S-PCN and 1 Au-6 T/6S-PCN samples were examined with transmission-electron-microscopy (TEM) and high-resolution TEM (HRTEM) images. The TEM image of PCN (Fig. 1C) clearly demonstrates that the sample exhibits porous structure and the diameter of pores fall in the range of 5–10 nm. The TEM image of 6S-PCN (Fig. 1D) shows that sulfur doping does not affect the morphology of PCN. The TEM micrographs of 6 T/6S-PCN and 1 Au-6 T/6S-PCN nanocomposites (Fig. 1E, F) reveal that TiO₂ nanoparticles with average diameter of 3–5 nm are well dispersed on the surface of 6S-PCN. The HRTEM micrograph of 1 Au-6 T/6S-PCN nanocomposite (Fig. 1G) shows that the lattice fringes with d-spacing 0.32 nm corresponds to the (101) facet of anatase TiO₂. The selected area electron diffraction (SAED) image of TiO₂ (Fig. 1G inset) clearly matches the pattern of TiO₂. The energy dispersive X-ray spectroscopy spectrum (Fig. 1H) shows the existence of C, N, S, Ti, and O elements. The EDS elemental mapping of 1 Au-6 T/6S-PCN composite Figure S3 (supporting information) further supports the TEM results. The distribution of carbon, nitrogen, sulfur, titanium, oxygen, can be clearly observed in Figure S3B–G (supporting

information). Since the Au concentration is $\sim 0.06\%$, well below the detection limit of XPS, TEM and EDS, it is not possible to map Au elements (supporting information, Figure S3 and the notes). Thus, it is clear that the heterojunctions between TiO_2 , Au- TiO_2 and 6S-PCN would be favorable for charge separation and transfer. From SEM image of PCN (Figure S4, Supporting Information), it is clear that the sample exhibit irregular porous hierarchical structure. Further, it is suggested that PCN nanosheets are interconnected and the irregularity of the pores are due to the escape of various gases during high temperature treatment.

The Nitrogen adsorption-desorption isotherm curve of PCN is shown in Figure S5 A (Supporting Information). It is demonstrated that the hysteresis loops of PCN are due to porous structure. The observed BET surface area of PCN is $\sim 100.5 \text{ m}^2 \text{ g}^{-1}$, which is remarkably higher than that of the previous reports [39]. The pore size diameter of PCN is in the range of 5–10 nm as confirmed by the desorption branch of Barrett-Joyner Halenda (BJH) method as shown in Figure S5B (Supporting Information). It is recommended that at relative low pressures, the isotherm maintain the shape of sharp capillary-condensation rung, which is attributed to the 3–10 nm pores. Further, at relatively high pressures the formed hysteresis loops are ascribed to the large size pores above 5 nm. Thus the resulting large surface-area and porous morphology would be favorable for the improved photocatalytic efficiency of CN.

In order to investigate the functional groups and surface chemical species of PCN, 6S-PCN, 6 T/6S-PCN and 1 Au-6 T/6S-PCN samples, Fourier-Transform-Infrared (FTIR) spectroscopy spectra were recorded as shown in Fig. 2A. The bands in the range of $1200\text{--}1600 \text{ cm}^{-1}$ are attributed to the stretching-modes of C–N heterocycles, while the band at 810 cm^{-1} corresponds to the vibration mode, and these are the characteristic absorption bands of triazine units. The bands in the range of $3000\text{--}3600 \text{ cm}^{-1}$ are assigned to the stretching-mode of N–H bond, as well as the adsorbed surface OH groups in C–N. It is obvious that the typical vibration bands of N–S are located at 700 cm^{-1} , and are mixed with vibration bands of the triazine rings [40]. A small band in the range of $2100\text{--}2300 \text{ cm}^{-1}$ is also detected which can be assigned to the stretching-modes between S and N.

To further confirm the chemical composition and elemental chemical-states of the samples, X-ray photoelectron-Spectroscopy (XPS) spectra were obtained. The XPS spectra of PCN, 6S-PCN, 6 T/6S-PCN and 1 Au-6 T/6S-PCN are shown in Figure S6 (Supporting Information). According to the Gaussian's rule, the high-resolution XPS of C1s are fitted into two peaks as shown in Figure S6A (Supporting Information). The peak at 284.4 eV corresponds to the C–C bond and originates from sp^2 C atoms bonded to the N atoms in the triazine rings (N–C=N). The peak at 287.2 eV is ascribed to the C=N bonds. The XPS spectra of N1s (Figure S6B, Supporting Information) are fitted into three components as shown in the inset figure. The peaks at 398, 400, and 403 eV ,

respectively are ascribed to the nitrogen atoms bonded to two carbon atoms (C–N = C) with sp^2 hybridization, tertiary nitrogen-groups N-(C)₃ as structural motif, or ((C)2NH) groups interlinked with structural-defects. But, in present case most of the N atoms are bonded to two S atoms. It is clear that the binding energy of nitrogen (N–S) is shifted toward lower energy side with increasing sulfur content. In fact, the electronegativity of N is higher than that of the sulfur, therefore the lone-pair electrons would transfer to N. However, the XPS peak intensity of N1s is unchanged while the intensity of C1s is decreased. Thus, it is confirmed that S2p replaces C1s from the ring of PCN. Fig. 2B shows the high-resolution spectra of S2p. It can be seen that xS-PCN samples exhibit a broad peak at $\sim 165.5 \text{ eV}$, suggesting that sulfur is successfully incorporated into the ring of PCN. According to Cheng and his workers [41], sulfur could substitute N from the ring and the binding energy of sulfur can be observed at 163.9 eV . However, in the present case, the higher binding energy ($\sim 165.5 \text{ eV}$) demonstrates that sulfur substitute carbon instead of nitrogen and form S–N bond. In fact, using ionic liquids, the substitution of carbon atoms by sulfur in graphitic carbon nitride has not been reported to till date. The XPS spectra of Ti2p for 6 T/6S-PCN and 1 Au-6 T/6S-PCN samples are given in Figure S6C (Supporting Information). It is clear that the binding energies of $\text{Ti}2\text{p}_{3/2}$ and $\text{Ti}2\text{p}_{1/2}$ for 6 T/6S-PCN sample are located at 458.1 eV and 463.8 eV respectively, which are attributed to the spin-orbital splitting of Ti^{4+} . Further, the Ti2p XPS peak of 1 Au-6 T/6S-PCN nanocomposite is slightly shifted toward the lower binding energy side compared to the 6 T/6S-PCN sample. This indicates that charge density is decreased in Au and increased in Ti2p as a result of the electronic redistribution when Au- TiO_2 is coupled with 6S-PCN sample. The XPS spectra of Au4f (Figure S6D, Supporting Information) demonstrate that the amount of Au is too small (0.06% of Au) which can be hardly detected. To further confirm the concentration of sulfur in xS-PCN samples, ICP-OES experiments were performed as shown in supporting information Table S1. The experimental values are consistent with the theoretical values.

The visible-light catalytic activities of the obtained samples were evaluated for CO_2 conversion and H_2 evolution as shown in Fig. 3 and Figure S7 (Supporting Information). From Figure S7A (Supporting Information), it is obvious that PCN exhibit weak activity for CO_2 photoreduction, however, it is remarkably improved after doping sulfur and the highest-activity is observed for 6S-PCN sample. Interestingly, the visible-light catalytic activity of 6S-PCN sample is further improved after coupling TiO_2 and Au- TiO_2 as shown in Fig. 3A. Noticeably, the 1 Au-6 T/6S-PCN nanocomposite exhibits the highest photoactivity ($365 \mu\text{mol g}^{-1} \text{ h}^{-1}$ of CH_4). During CO_2 conversion process, three types of gas phase products were detected (the major product CH_4 and minor products O_2 and CO). The calculated quantum efficiency for CO_2 conversion to CH_4 at 420 nm of PCN, 6S-PCN, 6 T/6S-PCN and 1 Au-6 T/6S-PCN samples are 1.10%, 1.89%, 3.87% and 4.67% respectively, which

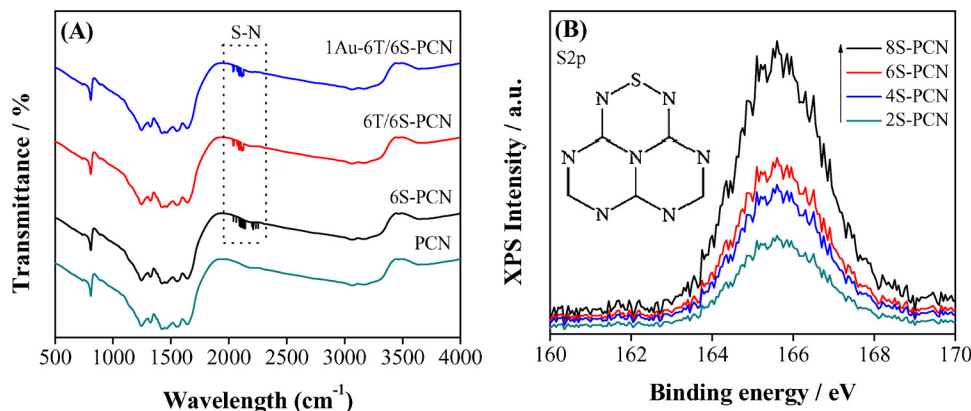


Fig. 2. FT-IR spectra (A) of PCN, 6S-PCN, 6 T/6S-PCN and 1 Au-6 T/6S-PCN, and S2p XPS spectra (B) of xS-PCN.

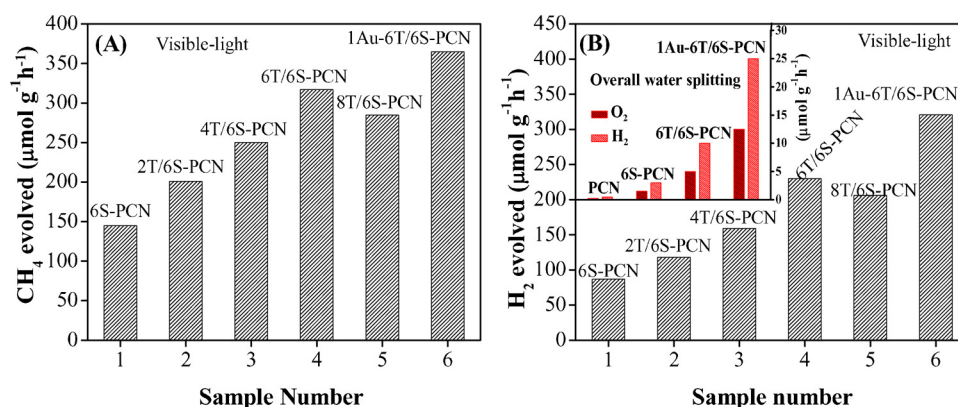


Fig. 3. Photocatalytic activities for CO₂ conversion to evolve CH₄ (A) and water splitting to evolve H₂ (B) of 6S-PCN, yT/6S-PCN, and 1 Au-6 T/6S-PCN. Inset of (B) overall water splitting of PCN, 6S-PCN, 6 T/6S-PCN and 1 Au-6 T/6S-PCN under visible-light irradiation.

is very close to natural photosynthesis.

To further confirm the improved visible-light photocatalytic activities for CO₂ reduction, we carried out H₂ evolution experiments of PCN, xS-PCN, yT/6S-PCN and 1 Au-6 T/6S-PCN samples under visible-light as shown in Fig. 3B and Figure S7B (Supporting Information). From Figure S7B (Supporting Information), it is clear that the visible-light activity of PCN for H₂ evolution is obviously enhanced after doping sulfur especially for the amount optimized 6S-PCN sample. Further, the activity of 6S-PCN for H₂ evolution is significantly improved after coupling TiO₂ and Au-TiO₂ and the highest photoactivity (330 μmol g⁻¹ h⁻¹) is observed for 1 Au-6 T/6S-PCN nanocomposite which is almost 41-time of the pure PCN. Further, we have measured the hourly production of H₂ and O₂ over the amount optimized 1 Au-6 T/6S-PCN nanocomposite in a single photocatalytic cycle as shown in Figure S8 (Supporting Information). It is confirmed that the steady H₂ and O₂ evolution ratio is 2:1. The calculated quantum efficiency of PCN, 6S-PCN, 6 T/6S-PCN and 1 Au-6 T/6S-PCN samples for water splitting to evolve H₂ at 420 nm, are respectively 0.54%, 1.78%, 2.56%, and 3.34%. The activity of our photocatalyst for water splitting to evolve H₂ and CO₂ conversion is much higher than the previous reports as shown in Table S2.

In addition, we have also measured the activity of the optimized PCN, 6S-PCN, 6 T/6S-PCN and 1 Au-6 T/6S-PCN samples for overall water splitting without adding any hole-sacrificing agent and co-catalyst. As shown in Fig. 3B inset, the activity of PCN for overall water splitting is negligible, however, after doping sulfur the activity is increased and further increased after coupling TiO₂ and Au-TiO₂. The photocatalytic activity of 1 Au-6 T/6S-PCN nanocomposite for overall water splitting is much significant. The overall water splitting experiments suggest that the design photocatalyst has enough ability to produce atomic hydrogen which may be used as an intermediate in the conversion of CO₂ to CH₄.

In order to confirm the CO₂ conversion products over 1 Au-6 T/6S-PCN nanocomposite, we have analyzed the photocatalytic products via gas chromatography-mass spectrometry (GC-MS) apparatus. As shown in Figure S9 (Supporting Information), after visible-light irradiation for 8 h, the peak at *m/z* value of 16 can be attributed to the CH₄, and the peaks at *m/z* values of 13, 14, and 15 can be assigned to the fragments of CH₄. The peaks at *m/z* values of 28 and 32 correspond to CO, and O₂ (oxidation production), respectively. The peak at *m/z* value of 44 is attributed to the CO₂ (raw material).

To check the long term stability of 1 Au-6 T/6S-PCN nanocomposite for CO₂ conversion and H₂ evolution, photocatalytic recyclable tests were measured as shown in Figure S10 (Supporting Information). It can be seen clearly that 1 Au-6 T/6S-PCN nanocomposite is capable of producing 1800 μmol CO₂ and 1600 μmol H₂ in 5 h. Further, no deactivation of the photocatalyst is observed even after 6 runs (each of 5 h). This shows that the 1 Au-6 T/6S-PCN nanocomposite is highly stable

and does not photocorrode during the photocatalytic reaction.

To further support the CO₂ conversion and water splitting experiments, we have measured the visible-light catalytic activity of PCN, xS-PCN, yT/6S-PCN and 1 Au-6 T/6S-PCN samples for 2,4-dichlorophenol degradation as shown in Figure S11 (Supporting Information). From Figure S11 A (Supporting Information), it is clear that PCN exhibits weak photoactivity (only 4%) for 2,4-DCP degradation after visible-light irradiation for 1 h. However, the photoactivity is obviously improved after doping sulphur, especially for the amount optimized 6S-PCN sample (48%). The activity is further improved after coupling TiO₂ and Au-TiO₂ as shown in Figure S11B (Supporting Information). Interestingly, the degradation rates for 6 T/6S-PCN and 1 Au-6 T/6S-PCN samples are 87% and 95% respectively. This shows that the photocatalysts not only exhibit high reduction ability but also have excellent oxidation ability.

It is widely accepted, that when a semiconductor is incident with proper energy photons, the absorbed photons produce charge carrier's (electron-hole pairs) in the region of surface and/or interface, which then transfer to the surface states. Thus, a substantial amount of the produced charge may transfer in opposite directions and build up electric fields thus change in the net surface charge would be expected. However, it is a big challenge to measure the solid-state photogenerated charge carrier's separation. For this, atmosphere-controlled steady-state surface photovoltage spectroscopy (SS-SPS) is the best technique. It is a highly sensitive and direct method used to reveal the surface charge properties of semiconductor solid materials. For semiconductor nanomaterials, the SS-SPS response mainly derives from photogenerated charge separation via diffusion process, since the built-in electric field is negligible. Generally, stronger is the SS-SPS response, higher is the photogenerated charge separation. From Figure S12 A (Supporting Information), it can be seen clearly that PCN exhibits weak SS-SPS signal which is attributed to the fast recombination rate of photogenerated charges. However, the SS-SPS response of PCN is obviously enhanced after doping sulfur especially for the amount optimized 6S-PCN sample. Further, from Fig. 4A, it is clear that the SS-SPS signal of 6S-PCN sample is greatly improved after coupling TiO₂ and 6 T/6S-PCN sample exhibits the highest signal. Interestingly, after coupling Au-TiO₂ the SS-SPS signal of 1 Au-6 T/6S-PCN nanocomposite is much stronger. Hence, it is suggested that charge separation is significantly improved. To clarify this, we have measured SS-SPS responses of the samples in different atmospheres. From Figure S12B (Supporting Information), it is obvious that the SS-SPS signal of PCN in different atmospheres is remarkably enhanced after doping sulfur. Moreover, after coupling TiO₂ and Au-TiO₂ the SS-SPS responses in different atmospheres are much significant as can be seen from Fig. 4B. The SS-SPS responses in different atmospheres are in the order O₂ < air < N₂. Particularly, the 1 Au-6 T/6S-PCN nanocomposite shows the highest SS-SPS even in different atmospheres. Based on the SS-SPS results, it is demonstrated

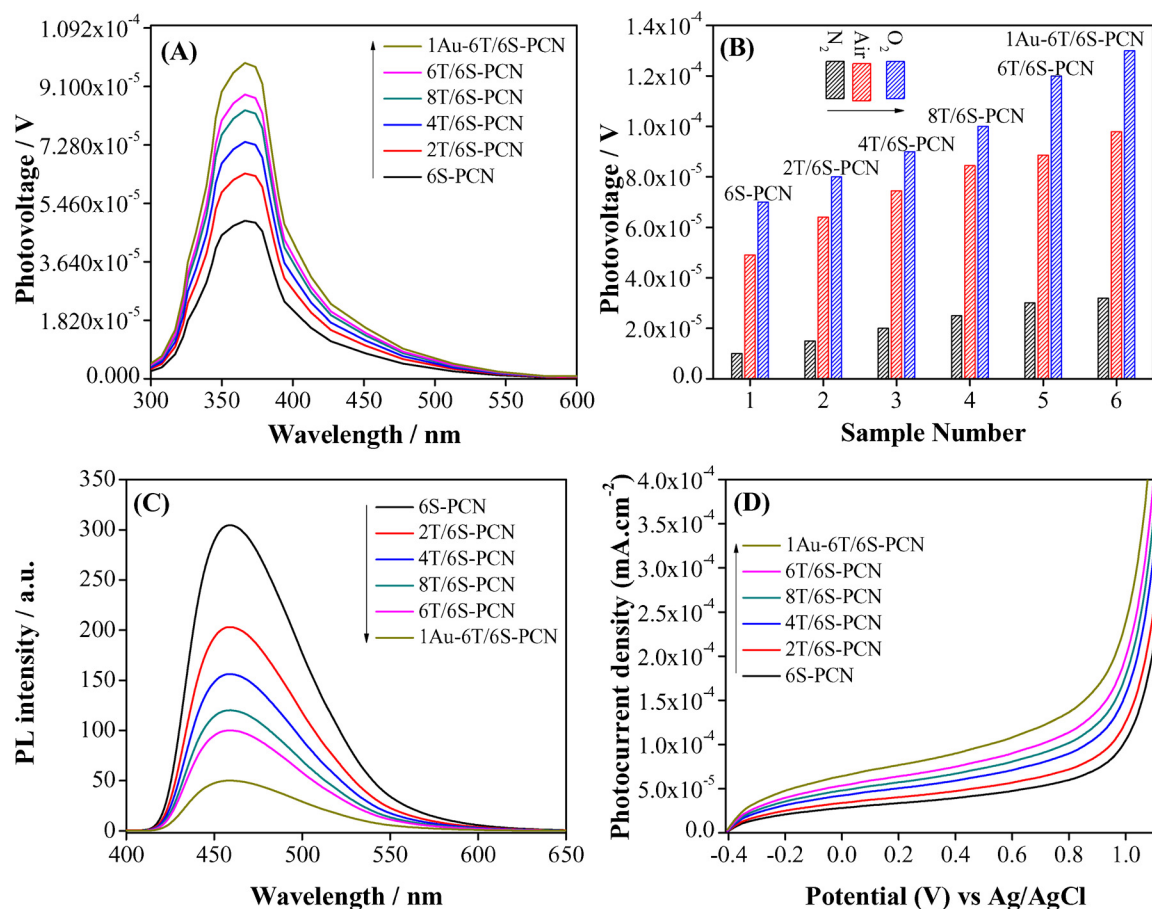


Fig. 4. SS-SPS responses in air (A), SPS peak intensities at 380 nm in different atmospheres (B), Photoluminescence spectra (C), and PEC I-V curves (D) of 6S-PCN, yT/6S-PCN and 1 Au-6 T/6S-PCN. Electrochemical performance was measured in a 0.5 M NaClO₄ solution, and Hg/Hg₂Cl₂ (saturated KCl) electrode was used as the reference electrode.

that photogenerated charge separation in PCN could be obviously improved after doping sulfur and then coupling TiO₂ and Au-TiO₂. This is attributed to the sulfur introduced surface states near the CBM of PCN that effectively captures photogenerated electrons and further attributed to the coupled TiO₂ that accepts the electron of PCN and Au. In this way, the charge recombination is effectively reduced.

The photoluminescence (PL) spectroscopy is also highly sensitive technique used to investigate the optical, electronic and photochemical properties as well as active sites on semiconductor surfaces. From PL, we can also get information about surface defects, oxygen vacancies, charge transfer, immigration and electron-hole pairs trapping efficiency. From Figure S13 (Supporting Information), it is clear that PCN exhibits a strong PL signal centring at approximately 460 nm, which is related to the optical energy band gap of 2.7 eV. The strong PL signal of PCN corresponds to the fast recombination rate of photogenerated charges. Obviously, the PL intensities of xS-PCN samples are greatly decreased and the lowest PL signal is observed for 6S-PCN sample. Moreover, the PL signals of yT/6S-PCN nanocomposites are considerably decreased and the lowest signal is detected for 1 Au-6 T/6S-PCN nanocomposites as shown in Fig. 4C. Hence, it is suggested that the charge carrier's recombination is significantly reduced.

To further confirm the enhanced charge separation, we have measured the photoelectrochemical I-V curves of the samples in 0.5 M Na₂SO₄ solution under visible-light irradiation. From Figure S14 (Supporting Information), it is obvious that the photocurrent density response of PCN is greatly enhanced after doping sulfur especially for the amount optimized 6S-PCN. As expected, after coupling TiO₂ and Au-TiO₂, the photocurrent density response of 6S-PCN sample is considerably enhanced and the highest photocurrent response is detected

for 1 Au-6 T/6S-PCN nanocomposite as shown in Fig. 4D. Obviously, the SS-SPS, PL and PEC responses well support the above photocatalytic activities.

To understand the related mechanism, we have measured photocatalytic activities for CO₂ conversion and water splitting under single wavelength irradiation (365–590 nm) as shown in Figures S15 and S16 (Supporting Information). It is clear that PCN shows an obvious photocatalytic activity for CO₂ conversion under the irradiation below 450 nm, while it exhibit weak photoactivity at wavelength 470 nm. As expected, the 1 Au-6 T/6S-PCN nanocomposite exhibits much high photoactivity upto 550 nm. This is attributed to the newly formed surface states related to sulfur near the conduction band bottom of PCN and further to the coupled Au-TiO₂. Further, to explore the charge separation and transfer properties of PCN, xS-PCN, yT/6S-PCN and 1 Au-6 T/6S-PCN samples, coumarin fluorescent method was used to detect the amount of produced hydroxyl radicals. In coumarin fluorescent method, the coumarin reacts with OH and produce luminescent 7-hydroxycoumarin. Generally, the stronger is the fluorescent signal, the larger is the produced OH amount. The amounts of produced OH by the samples is shown in Fig. 5A and Figure S17 (Supporting Information). It is demonstrated that PCN exhibits a low amount of OH, while for xS-PCN samples, the produced OH amounts are considerably higher. Further enhancement in OH amount is observed for yT/6S-PCN, especially for the amount optimized 6 T/6S-PCN sample. Interestingly, the highest amount of OH is detected for 1 Au-6 T/6S-PCN nanocomposite.

In order to reveal the extended visible-light absorption, improved charge separation and visible-light activities, we have measured single wavelength photocurrent action spectra of PCN, 6S-PCN, 6 T/6S-PCN and 1 Au-6 T/6S-PCN samples as a function of different excitation

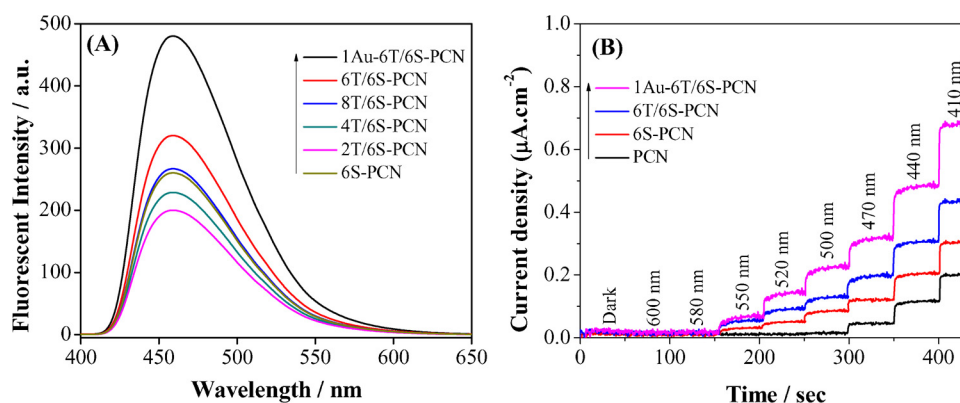


Fig. 5. Fluorescence spectra related to OH radical amount (A) of 6S-PCN, yT/6S-PCN and 1 Au-6 T/6S-PCN samples, and Single wavelength PEC (B) of PCN, 6S-PCN, 6 T/6S-PCN and 1 Au-6 T/6S-PCN.

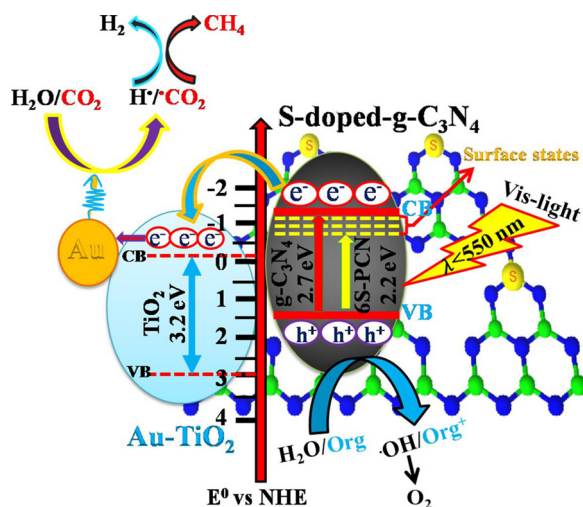


Fig. 6. Schematic of the energy bandgap, photogenerated charge separation and transfer, and the visible-light photocatalytic processes over 1 Au-6 T/6S-PCN nanocomposite.

wavelengths in 0.5 M Na₂SO₄ solution at 0.3 V bias vs Ag/AgCl electrode. From Fig. 5B, it is clear that PCN exhibit photocurrent response at 470 nm. This is in accordance with the energy band gap (2.7 eV) of PCN. As expected, the photocurrent response for 6S-PCN sample appeared at 550 nm. This threshold wavelength is closely related to electronic transition in semiconductor with energy band gap of ~ 2.2 eV. Interestingly, the photocurrent intensity of 6 T/6S-PCN sample is remarkably enhanced and further enhancement is observed for the 1 Au-6 T/6S-PCN nanocomposite. To well understand the enhanced visible-light activities of 1 Au-6 T/6S-PCN nanocomposite, a schematic mechanism is proposed as shown in the Fig. 6. It is clear that the VBM and CBM of PCN are located at 1.4 and -1.3 eV, respectively. As observed, the visible-light absorption of PCN is extended after doping a proper amount of sulfur. This is attributed to the newly introduced surface states related to sulfur near the CB bottom of PCN. These surface states could effectively capture photogenerated electrons so as to promote the charge separation. Thus, it is clear that the visible-light response of PCN could be extended from 470 to 550 nm by shifting its CB downward to a certain degree (-0.6 eV) after doping a proper amount of sulfur. As a result, the charge separation will be greatly improved. However, the over excess amount is unfavorable because the surface states with low energy levels acts as charge recombination center. Further, it is confirmed that when TiO₂ is coupled with 6S-PCN, the visible-light excited electrons of 6S-PCN would transfer to the CB of TiO₂ leading to the enhanced charge separation and hence visible-light activities. Moreover, it is demonstrated that when heterojunction is

formed between Au-TiO₂ and 6S-PCN, the Au-TiO₂ would accept the visible-light excited electrons of 6S-PCN and then provide catalytic functions to the reduction reactions with CO₂ and H₂O. In CO₂ photo-reduction, the induced electrons could directly initiate reduction reactions with CO₂ to produce $\cdot\text{CO}_2$. Similarly, the electrons could induce reduction reactions with H₂O to produce $\cdot\text{H}$, and then to evolve H₂. Thus, the $\cdot\text{H}$ would directly attack $\cdot\text{CO}_2$ and produce CH₄. Meanwhile, the photogenerated holes would initiate the oxidation reactions with H₂O to produce $\cdot\text{OH}$, and then to evolve O₂.

3. Conclusion

In summary, a novel visible-light responsive Au-T/S-PCN nanocomposite has been successfully fabricated. The resultant nanocomposites exhibit exceptional cocatalyst-free visible-light photocatalytic activities for CO₂ conversion (32-time), H₂ evolution (41-time) and 2,4-DCP degradation (24-time) compared to the unmodified PCN. It is clearly demonstrated that the enhanced photocatalytic activities of 1 Au-6 T/6S-PCN nanocomposite are attributed to the extended visible-light absorption after doping sulfur to create surface states near the CB of PCN, and further to the greatly promoted charge separation by coupling Au-TiO₂. The quantum efficiencies of the designed nanocomposite for CO₂ conversion and water splitting are approximately ~4.67% and 3.34% at wavelength 420 nm, which are much higher than the other reported values. This work provides new routes to design g-C₃N₄-based nanophotocatalysts for efficient CO₂ conversion, water splitting and 2,4-DCP degradation, and could be extended to other nanophotocatalysts for effective solar energy utilization.

4. Experimental section

All the reagents were of analytical grade and used as-received without further purification. Deionized water was used throughout the experiments.

4.1. Synthesis of porous g-C₃N₄ (PCN) and sulfur-doped g-C₃N₄ (S-PCN)

Porous CN was synthesized according to the following procedure. In a typical synthesis, 10 g melamine was dispersed into 500 mL C₂H₅OH containing 6 g of cyanuric acid. The suspension was continuously stirred at 60 °C for 24 h, then centrifuged and dried in oven at 80 °C. The obtained powder was then annealed at 520 °C (1 °C min⁻¹ in N₂) for 4 h. Finally, the resulting yellow-colored product was washed several times with boiling H₂O to remove the residual cyanuric acid, and finally dried at 100 °C over night. For sulfur doping same procedure was used however, ionic liquid (1-butyl-3-methylimidazolium thiocyanate) [BMIM][SCN] was added as a source of sulfur. The sulfur doped samples are represented by xS-PCN (where x means 2, 4, 6 and 8 mol ratio

% of the used sulphur).

4.2. Synthesis of TiO_2 and Au- TiO_2

TiO_2 was synthesized by a sol-thermal method. In a typical process, 5 mL of butyl titanate was dissolved into a mixed solvent of 5 mL anhydrous ethanol (99.7%) and 2.5 mL deionized H_2O . At the same time, 1 mL HNO_3 (67%) was mixed with 20 mL of anhydrous $\text{C}_2\text{H}_5\text{OH}$. Then, the solution of butyl titanate was added drop-wise to the HNO_3 solution under stirring. After stirring for 1 h, a semi-transparent sol was obtained. Then, the resulting sol was transferred into a stainless-steel autoclave and heated at 160°C for 6 h. When room temperature was attained, the product was centrifuged and washed several times with absolute $\text{C}_2\text{H}_5\text{OH}$ and finally dried in oven at 80°C . The product was crushed and annealed at 450°C in air for 2 h to obtain the nanocrystalline anatase TiO_2 . To obtain Au- TiO_2 sample, same procedure was used. However, 1 mol ratio % of Au solution was added to the TiO_2 precursor [42].

4.3. Fabrication of nanocomposites

To fabricate different mass ratio percentage TiO_2 coupled 6S-PCN (yT/6S-PCN) nanocomposites, 1 g of the freshly prepared 6S-PCN was taken and dissolved into a mixture of 2.5 mL distilled H_2O , 0.5 mL HNO_3 , and 10 mL $\text{C}_2\text{H}_5\text{OH}$. Then the mixture was stirred for 1 h. After that, different mass-ratio percentage (2, 4, 6, and 8%) of TiO_2 was added to it. The mixture was continuously stirred for 2 h, and subsequently dried at 80°C . Finally annealed at 500°C for 2 h, yT/6S-PCN nanocomposites were obtained, in which y means the mass-ratio percentage of TiO_2 to 6S-PCN. To prepare 1 Au-6 T/6S-PCN nanocomposite, same procedure was used but 6% Au- TiO_2 was coupled with 6S-PCN sample instead of common TiO_2 .

4.4. Materials characterization

XRD patterns of PCN, xS-PCN, yT/6S-PCN, and 1 Au-6 T/6S-PCN samples were measured with XRD (Bruker D8, Germany). UV-vis diffuse-reflectance spectra (DRS) were measured with UV-2550 spectrometer (Shimadzu Japan). TEM and HRTEM images were obtained with a JEOL JEM-2100 transmission-electron microscope (TEM) operated at 200 kV. Fourier transform infrared (FT-IR) spectroscopy spectra in the range of $400\text{--}4000\text{ cm}^{-1}$ were obtained in KBr diluent with Shimadzu-IR Prestige-21. X-ray photoelectron spectroscopy (XPS) spectra were obtained with a Kratos-Axis Ultra DLD apparatus having Al (mono) X-ray source. The concentration of sulfur was measured with ICP-OES (PerkinElmer 8000). The N_2 adsorption-desorption isotherm curves were measured with Micromeritics ASAP-2020 M system at the temperature of liquid N_2 , while prior to measurements, the system was outgassed for 10 h at 300°C . The BET surface area was measured with a constant volume adsorption apparatus ST-2000. The steady-state surface-photovoltage spectroscopy (SS-SPS) analysis was performed with home-built equipment, having a lock-in amplifier (SR830) synchronized with a light chopper (SR540). Powder form of the sample was pasted between two indium tin-oxide (ITO) glass electrodes and then kept in atmosphere-controlled equipment. A 500 W xenon lamp (CHF XQ500 W, Global xenon lamp power) was used as a light source. To obtain a monochromatic light, double prism monochromator (SBP300) was used. The photoluminescence (PL) spectra were recorded with a PE-LS-55 spectro-fluoro photometer with excitation wavelength of 390 nm.

4.5. Evaluation of photocatalytic activities for CO_2 conversion

In a typical CO_2 experiment, 0.1 g of the sample was dispersed in 3 mL H_2O contained in a 100 mL volume cylindrical steel-reactor with area 3.5 cm^2 . The radiation source was a 300 W Xenon lamp with cut-off

filter 420 nm. During the experiment, high-purity CO_2 gas was passed through H_2O system and then entered into the reaction setup to gain ambient pressure. Prior to irradiation, the $\text{CO}_2/\text{H}_2\text{O}$ system was equilibrated in the presence of photocatalyst for 1 h. During the photocatalytic process, 0.5 mL of the gas was regularly taken with a syringe from the reactor at given time interval for the detection of CO , O_2 and CH_4 concentration with a gas chromatograph (Tech, GC-7900, nitrogen gas carrier and GC-2014 with FID detector; Shimadzu Corp., Japan).

4.6. Evaluation of photocatalytic activities for H_2 evolution

The H_2 evolution experiments were performed in an online cylindrical quartz cell (250 mL volume and 7.5 cm^2 area) connected to a tightly closed gas circulation system. The evolved gases were detected with an online TCD gas-chromatograph (Tech, GC-7900, nitrogen gas carrier). About 0.1 g of the sample was dispersed in a mixture of 80 mL distilled H_2O and 20 mL CH_3OH (in overall water splitting 100 mL H_2O was used). The mixture was thoroughly irradiated by a 300 W xenon lamp with a cut-off filter of 420 nm. The amount of evolved H_2 gas was measured after regular time interval (1 h) under visible-irradiation [43].

4.7. Evaluation of photocatalytic activities for 2,4-DCP degradation

The experiments for 2,4-dichlorophenol (2,4-DCP) degradation were performed in a 150 mL glass-reactor. A high pressure Xenon lamp 150 W GYZ220 (made in China) with a cut-off filter (420 nm) was used as the radiation source. For each experiment, 0.1 g of each sample was dispersed in 80 mL of 10 mg/L 2,4-DCP solution under stirring for half an hour in dark to reach the adsorption-desorption equilibrium. After that, the solution was continuously irradiated for 1 h, then centrifuged and the concentration of 2,4-DCP was measured with a Model Shimadzu UV-2550 spectrophotometer at the characteristic optical adsorption of 285 nm.

4.8. Measurement of the $\cdot\text{OH}$ amount

In a typical experiment, 0.05 g of the powder sample was dispersed in 40 mL of 0.001 M coumarin aqueous solution taken in a quartz reactor. Before irradiation, the system was continuously stirred for half an hour to reach the adsorption-desorption equilibrium. After that, the sample was irradiated for 1 h and the desired amount was centrifuged and a specific volume was tested for the fluorescence measurement of 7-hydroxycoumarin with the help of a spectrofluorometer (Perkin-Elmer LS 55). During measurement, the excitation wavelength was fixed at 390 nm and emission-wavelength was kept at 460 nm [38].

4.9. Photoelectrochemical (PEC) measurements

The PEC experiments were conducted according to our previous report [38]. In each experiment, 0.05 g of the catalyst was dispersed in 2 mL isopropyl-alcohol under stirring. Then, 0.025 g of Macrolog-6000 was added to it and kept under ultrasonic treatment for 30 min. After that, 0.05 mL of acetyl-acetone was added to it and continuously stirred for three days. The freshly cleaned conductive-fluorine doped tin-oxide (FTO) coated glasses were used as substrate for films making. The as-prepared films by doctor blade method were first dried in air and then annealed at 450°C for half an hour. After annealing, the FTO coated glasses were cut into $1.0\text{ cm} \times 3.0\text{ cm}$ pieces with film surface area of $1.0\text{ cm} \times 1.0\text{ cm}$. During PEC measurement, an electrical contact was made with electrode film by a silver-conducting paste connected to a copper-wire enclosed in a glass tube. The working arithmetic surface-area of the film was $0.5\text{ cm} \times 0.5\text{ cm}$ [44,45]. PEC measurements were carried out in a three-electrode configuration system and 0.5 M Na_2SO_4 was used as electrolyte. The film acts as a working electrode, Ag/AgCl as a reference electrode, and Pt plate as the counter electrode.

Acknowledgements

The work was financially supported by the National Natural Science Foundation of China (No. 11574106, 61771448, 51635007, 21571064, 21371060), the China Postdoctoral Science Foundation under Grant no. 2017M622404, and the Fundamental Research Projects of Shenzhen City: JCYJ20150831202835225.

Appendix A. Supplementary data

Supplementary material related to this article can be found, in the online version, at doi:<https://doi.org/10.1016/j.apcatb.2018.06.009>.

References

- [1] B. Kumar, M. Asadi, D. Pisasale, S. Sinha-Ray, B.A. Rosen, R. Haasch, J. Abiade, A.L. Yarin, A. Salehi-Khojin, Renewable and metal-free carbon nanofibre catalysts for carbon dioxide reduction, *Nat. Commun.* 4 (2013) 3819.
- [2] D. Chen, H. Zhang, Y. Liu, J. Li, Graphene and its derivatives for the development of solar cells, photoelectrochemical, and photocatalytic applications, *Energy Environ. Sci.* 6 (2013) 1362.
- [3] D. Deng, K. Novoselov, Q. Fu, N. Zheng, Z. Tian, X. Bao, Catalysis with two-dimensional materials and their heterostructures, *Nat. Nanotechnol.* 11 (2016) 218.
- [4] L. Weng, H. Zhang, A.O. Govorov, M. Ouyang, Hierarchical synthesis of non-centrosymmetric hybrid nanostructures and enabled plasmon-driven photocatalysis, *Nat. Commun.* 5 (2014) 5792.
- [5] K.T. Ngo, M. McKinnon, B. Mahanti, R. Narayanan, D.C. Grills, M.Z. Ertem, J. Rochford, Turning on the protonation-first pathway for electrocatalytic CO₂ reduction by manganese bipyridyl tricarbonyl complexes, *J. Am. Chem. Soc.* 139 (2017) 2604.
- [6] D. Gao, Y. Zhang, Z. Zhou, F. Cai, X. Zhao, W. Huang, Y. Li, J. Zhu, P. Liu, F. Yang, Enhancing CO₂ electroreduction with the metal-oxide interface, *J. Am. Chem. Soc.* 139 (2017) 5652.
- [7] S. Chu, A. Majumdar, Opportunities and challenges for a sustainable energy future, *Nature* 488 (2012) 294–303.
- [8] A.C. Janetos, Energy infrastructure: mapping future electricity demand, *Nat. Energy* 1 (2016) 16116.
- [9] K. Niu, Y. Xu, H. Wang, R. Ye, H.L. Xin, F. Lin, C. Tian, Y. Lum, K.C. Bustillo, M.M. Doeff, A spongy nickel-organic CO₂ reduction photocatalyst for nearly 100% selective CO production, *Sci. Adv.* 3 (2017) e1700921.
- [10] J.A. Herron, J. Kim, A.A. Upadhye, G.W. Huber, C.T. Maravelias, A general framework for the assessment of solar fuel technologies, *Energy Environ. Sci.* 8 (2015) 126.
- [11] L. Li, X. Mu, W. Liu, Z. Mi, C.-J. Li, Simple and efficient system for combined solar energy harvesting and reversible hydrogen storage, *J. Am. Chem. Soc.* 137 (2015) 7576.
- [12] D.M. Schultz, T.P. Yoon, Solar synthesis: prospects in visible light photocatalysis, *Science* 343 (2014) 1239176.
- [13] M. Humayun, Y. Qu, F. Raziq, R. Yan, Z. Li, X. Zhang, L. Jing, Exceptional visible-light activities of TiO₂-coupled N-doped porous perovskite LaFeO₃ for 2, 4-dichlorophenol decomposition and CO₂ conversion, *Environ. Sci. Technol.* 50 (2016) 13600.
- [14] Y.-X. Pan, Y. You, S. Xin, Y. Li, G. Fu, Z. Cui, Y.-L. Men, F.-F. Cao, S.-H. Yu, J.B. Goodenough, Photocatalytic CO₂ reduction by carbon-coated indium-oxide nanobelts, *J. Am. Chem. Soc.* 139 (2017) 4123.
- [15] W. Luc, C. Collins, S. Wang, H. Xin, K. He, Y. Kang, F. Jiao, Ag–Sn bimetallic catalyst with a core-shell structure for CO₂ reduction, *J. Am. Chem. Soc.* 139 (2017) 1885.
- [16] K.G. Laurier, F. Vermoortele, R. Ameloot, D.E. De Vos, J. Hofkens, M.B. Roeffaers, Iron (III)-based metal-organic frameworks as visible light photocatalysts, *J. Am. Chem. Soc.* 135 (2013) 14488.
- [17] Y. Zheng, L. Lin, X. Ye, F. Guo, X. Wang, Helical graphitic carbon nitrides with photocatalytic and optical activities, *Angew. Chem.* 126 (2014) 12120.
- [18] Z. Zhao, Y. Sun, F. Dong, Graphitic carbon nitride based nanocomposites: a review, *Nanoscale* 7 (2015) 15.
- [19] F. Raziq, L. Sun, Y. Wang, X. Zhang, M. Humayun, S. Ali, L. Bai, Y. Qu, H. Yu, L. Jing, Synthesis of large surface-area g-C₃N₄ comodified with MnO_x and Au-TiO₂ as efficient visible-light photocatalysts for fuel production, *Adv. Energy Mater.* 8 (2018) 1701580.
- [20] J. Liang, Y. Jiao, M. Jaroniec, S.Z. Qiao, Sulfur and nitrogen dual-doped mesoporous graphene electrocatalyst for oxygen reduction with synergistically enhanced performance, *Angew. Chem. Int. Ed.* 51 (2012) 11496.
- [21] Z. Ma, S. Dou, A. Shen, L. Tao, L. Dai, S. Wang, Sulfur-doped graphene derived from cycled lithium-sulfur batteries as a metal-free electrocatalyst for the oxygen reduction reaction, *Angew. Chem. Int. Ed.* 54 (2015) 1888.
- [22] L. Zhou, H. Zhang, H. Sun, S. Liu, M.O. Tade, S. Wang, W. Jin, Recent advances in non-metal modification of graphitic carbon nitride for photocatalysis: a historic review, *Catal. Sci. Technol.* 6 (2016) 7002.
- [23] J. Hong, X. Xia, Y. Wang, R. Xu, Mesoporous carbon nitride with in situ sulfur doping for enhanced photocatalytic hydrogen evolution from water under visible light, *J. Mater. Chem.* 22 (2012) 15006.
- [24] C. Xu, Q. Han, Y. Zhao, L. Wang, Y. Li, L. Qu, Sulfur-doped graphitic carbon nitride decorated with graphene quantum dots for an efficient metal-free electrocatalyst, *J. Mater. Chem. A* 3 (2015) 1841.
- [25] F. Wu, Y. Yu, H. Yang, L.N. German, Z. Li, J. Chen, W. Yang, L. Huang, W. Shi, L. Wang, Simultaneous enhancement of charge separation and hole transportation in a TiO₂-SrTiO₃ core-shell nanowire photoelectrochemical system, *Adv. Mater.* 29 (2017) 1701432.
- [26] V.S. Becerril, E. Sundin, M. Mapar, M. Abrahamsson, Extending charge separation lifetime and distance in patterned dye-sensitized SnO₂-TiO₂ μm-thin films, *Phys. Chem. Chem. Phys.* 19 (2017) 22684.
- [27] C. Ye, J.-X. Li, Z.-J. Li, X.-B. Li, X.-B. Fan, L.-P. Zhang, B. Chen, C.-H. Tung, L.-Z. Wu, Enhanced driving force and charge separation efficiency of protonated g-C₃N₄ for photocatalytic O₂ evolution, *ACS Catal.* 5 (2015) 6973.
- [28] Q. Yao, C. Wang, H. Wang, H. Yan, J. Lu, Revisiting the Au particle size effect on TiO₂-coated Au/TiO₂ catalysts in CO oxidation reaction, *J. Phys. Chem. C* 120 (2016) 9174.
- [29] J. Twilton, P. Zhang, M.H. Shaw, R.W. Evans, D.W. MacMillan, The merger of transition metal and photocatalysis, *Nat. Rev. Chem.* 1 (2017) 41017–41570.
- [30] H. Park, H.-i. Kim, G.-h. Moon, W. Choi, Photoinduced charge transfer processes in solar photocatalysis based on modified TiO₂, *Energy Environ. Sci.* 9 (2016) 411.
- [31] S. Chen, T. Takata, K. Domen, Particulate photocatalysts for overall water splitting, *Nat. Rev. Mater.* 2 (2017) 201750.
- [32] J. Wang, L. Huang, R. Yang, Z. Zhang, J. Wu, Y. Gao, Q. Wang, D. O'Hare, Z. Zhong, Recent advances in solid sorbents for CO₂ capture and new development trends, *Energy Environ. Sci.* 7 (2014) 3478–3518.
- [33] J. Zhang, Y. Chen, X. Wang, Two-dimensional covalent carbon nitride nanosheets: synthesis, functionalization, and applications, *Energy Environ. Sci.* 8 (2015) 3092–3108.
- [34] X. Chang, T. Wang, J. Gong, CO₂ photo-reduction: insights into CO₂ activation and reaction on surfaces of photocatalysts, *Energy Environ. Sci.* 9 (2016) 2177.
- [35] Z.-Z. Yang, L.-N. He, J. Gao, A.-H. Liu, B. Yu, Carbon dioxide utilization with C–N bond formation: carbon dioxide capture and subsequent conversion, *Energy Environ. Sci.* 5 (2012) 6602.
- [36] J. Fessler, J.H. Jeoung, H. Dobbek, How the [NiFe₂S₄] cluster of CO dehydrogenase activates CO₂ and NCO[−], *Angew. Chem. Int. Ed.* 54 (2015) 8560.
- [37] Q. Xiang, B. Cheng, J. Yu, Graphene-based photocatalysts for solar-fuel generation, *Angew. Chem. Int. Ed.* 54 (2015) 11350.
- [38] F. Raziq, Y. Qu, M. Humayun, A. Zada, H. Yu, L. Jing, Synthesis of SnO₂/BP co-doped g-C₃N₄ nanocomposites as efficient cocatalyst-free visible-light photocatalysts for CO₂ conversion and pollutant degradation, *Appl. Catal. B: Environ.* 201 (2017) 486.
- [39] Y. Zheng, L. Lin, B. Wang, X. Wang, Graphitic carbon nitride polymers toward sustainable photoredox catalysis, *Angew. Chem. Int. Ed.* 54 (2015) 12868.
- [40] C. Hampton, D. Demoin, R.E. Glaser, Vibrational spectroscopy tutorial: sulfur and phosphorus, University of Missouri, Fall, 2010.
- [41] G. Liu, P. Niu, C. Sun, S.C. Smith, Z. Chen, G.Q. Lu, H.-M. Cheng, Unique electronic structure induced high photoreactivity of sulfur-doped graphitic C₃N₄, *J. Am. Chem. Soc.* 132 (2010) 11642.
- [42] J. Bian, Y. Qu, R. Fazal, X. Li, N. Sun, L. Jing, Accepting excited High-energy-level electrons and catalyzing H₂ evolution of dual-functional Ag-TiO₂ modifier for promoting visible-light photocatalytic activities of nanosized oxides, *J. Phys. Chem. C* 120 (2016) 11831.
- [43] M. Humayun, A. Zada, Z. Li, M. Xie, X. Zhang, Y. Qu, F. Raziq, L. Jing, Enhanced visible-light activities of porous BiFeO₃ by coupling with nanocrystalline TiO₂ and mechanism, *Appl. Catal. B: Environ.* 180 (2016) 219.
- [44] M. Humayun, Z. Li, L. Sun, X. Zhang, F. Raziq, A. Zada, Y. Qu, L. Jing, Coupling of nanocrystalline anatase TiO₂ to porous nanosized LaFeO₃ for efficient visible-light photocatalytic degradation of pollutants, *Nanomaterials* 6 (2016) 22.
- [45] M. Humayun, N. Sun, F. Raziq, X.L. Zhang, R. Yan, Z.J. Li, Y. Qu, L.Q. Jing, Synthesis of ZnO/Bi-doped porous LaFeO₃ nanocomposites as highly efficient nanophotocatalysts dependent on the enhanced utilization of visible-light-excited electrons, *Appl. Catal. B: Environ.* 231 (2018) 23.